Nanotechnology

PAPER • **OPEN ACCESS**

2D TMDC aging: a case study of monolayer WS_2 and mitigation strategies

To cite this article: P-J Wyndaele *et al* 2024 *Nanotechnology* **35** 475702

OPEN ACCESS
IOP Publishing
Nanotechnology

Nanotechnology **35** (2024) 475702 (10pp)
https://doi.org/10.1088/1361-6528/ad72fb

2D TMDC aging: a case study of monolayer WS_2 and mitigation strategies

P-J Wyndaele[1,2,*], J-F de Marneffe[2], R Slaets[1], B Groven[2], A Franquet[2], P Brüner[3], T Grehl[3] and S De Gendt[1,2]

[1] Katholieke Universiteit Leuven, 3000 Leuven, Belgium
[2] imec, 3001 Heverlee, Belgium
[3] IONTOF GmbH, 48149 Münster, Germany

E-mail: Pieter-Jan.Wyndaele@imec.be

Received 31 May 2024, revised 21 July 2024
Accepted for publication 23 August 2024
Published 3 September 2024

Abstract

Due to their unique properties, two-dimensional transition metal dichalcogenides (2D TMDCs) are considered for diverse applications in microelectronics, sensing, catalysis, to name a few. A common challenge in 2D TMDC research is the film's inherent instability i.e. spontaneous oxidation upon ambient exposure. The present study systematically explores the effect aging on the film composition and photoluminescent properties of monolayer WS_2, synthetically grown by metal-organic chemical vapor deposition. The aging rate is investigated for different oxygen- (i.e. O_2 gas concentration and humidity) and light-controlled environments. Simple mitigation strategies that do not involve capping the 2D TMDC layer are discussed, and their effectiveness demonstrated by benchmarking the evolution in photoluminescence response against ambient exposed monolayer WS_2. These results highlight the need to store 2D TMDCs in controlled environments to preserve the film quality and how future studies can account for the aging effect.

Supplementary material for this article is available online

Keywords: two dimensional materials, transition metal dichalcogenides, tungsten disulfide, aging

1. Introduction

Two-dimensional transition metal dichalcogenides (2D TMDCs), typically illustrated as MX_2 (M = W, Mo, … & X = S, Se, …), have been the focus of substantial research work owing to their interesting properties and broad range of applications e.g. microelectronics [1, 2] and catalysis [3, 4]. A common challenge in 2D TMDC research is the film's inherent instability i.e. spontaneous oxidation upon ambient exposure. Spontaneous ambient oxidation or 'aging' is known to be a photo-induced process [5], which requires both an oxygen source (e.g. O_2 gas, moisture) and light. Kotsakidis *et al* [5] reported that the oxidation of monolayer WS_2 only occurs when the absorbed light has a wavelength that exceeds the threshold energy for electronic excitation, demonstrating the photo-induced nature of aging process. Chang *et al* [6] proposed an oxidation mechanism that initiates after monolayer WS_2 absorbs a photon that induces an excitation event, generating an electron—hole pair. The excited electrons residing in the $WS_{2\ \text{conduction band}}$ (−5.6 eV vs vacuum level) transfer and reduce physisorbed O_2 gas, forming a superoxide $\bullet O_2^-$ ($O_2/\bullet O_2^-$ reduction potential energy: −4.1 eV vs. vacuum). The generated oxygen radicals bind to tungsten

* Author to whom any correspondence should be addressed.

atoms in sulfur vacancies, grain boundaries or at the edge of the film. Edge oxidation as onset of aging has been reported both theoretically [7] and experimentally [5, 8]. Basal plane oxidation, although thermodynamically favorable, suffers from a large kinetic barrier [9–11]. The kinetic barrier for O_2 dissociative adsorption is also chalcogen dependent, where faster oxidation kinetics were observed for Te $>$ Se $>$ S [12]. Liu *et al* [13] explained the chalcogen effect on the basis of decreasing chalcogen electronegativity, resulting in a more efficient electron transfer to the adsorbed O_2 molecule. Mitigation of 2D TMDC aging is critical to preserve film quality and prevent aging interfering as background effect.

Many 2D TMDC-focused studies rely on steady-state photoluminescence (PL) spectroscopy because of its versatility in detecting defects, doping densities, strain, etc with exceptional sensitivity [14]. 2D TMDC aging has been associated with a diminishing PL response [15, 16]. In contrast, other studies focusing on oxygen doping [15] or defect passivation using an oxygen plasma [17] reported an enhancement in PL emission. This raises the question of how oxygen incorporation through aging precisely affects the PL properties of the 2D TMDC film.

In this study, the effect aging on metal-organic chemical vapor deposited (MOCVD) monolayer WS_2 is systematically evaluated by monitoring the evolution in PL response and film composition. The aging rate is studied under different light- and oxygen-controlled conditions, including humidity and O_2 gas concentration. Simple protocols to mitigate aging are discussed and their effectiveness demonstrated by benchmarking the evolution in PL response against ambient exposed monolayer WS_2. These results highlight the importance of a controlled storage environment to preserve 2D TMDC quality and how future studies can account for the aging effect.

2. Results and discussion

2.1. Aging of MOCVD grown WS_2

An extremely surface sensitive technique is imperative to monitor the gradual sulfur by oxygen substitution in a 2D TMDC monolayer. Low energy ion scattering (LEIS) is a surface analytical technique that uses low energy ions in the keV range. The low energy ions do not penetrate the sample, but interact i.e. scatter off the outermost atomic layer. Hence, LEIS provides a highly quantitative analysis with extreme surface sensitivity [18]. Figure 1 shows the change in surface composition over 2.5 months, during which the WS_2 film is exposed to ambient atmosphere and daylight (ambient-1, methods). The backscattered ion yields indicate three different elements that remain constant, increase, and decrease over time. These backscattered ion yields are assigned to tungsten, oxygen, and sulfur, respectively, given the nature of the aging process i.e. gradual replacement of sulfur by oxygen atoms that bind to the tungsten transition metal. However, the backscattered tungsten ion yield shows the highest intensity, even at the start of the experiment, although the incident ion's field of view comprises of a one-to-one W/S ratio, as illustrated in figure 1. The higher backscattered ion yield is explained by tungsten's larger atomic mass, which results in a higher scattering energy, greater differential scattering cross section, and thus a larger backscattered ion yield [19, 20]. The same rationale explains why at the end of the experiment, when all sulfur is substituted by oxygen, the final oxygen ion yield is lower compared to the starting sulfur ion yield.

2.2. Effect of WS_2 aging on photoluminescent properties

Aging affects the WS_2 film composition and properties [21]. Monolayer WS_2 has an exceptional PL response, owing to the indirect–direct bandgap transition going from multi- to mono-layer thickness, yielding promising applications such as photodetector, flexible nanoelectronics, light emitter, to name a few. While some studies report oxygen incorporation enhances PL emission [15, 17], others claim it degrades its PL properties [16]. A 300 mm wafer of monolayer WS_2 grown via MOCVD on 90 nm SiO_2 is cut into coupons and left in a controlled lab environment while continuously exposed to light (ambient-2, methods). The effect of aging is evaluated by sporadically measuring three spectra on a coupon for statistics, which is trashed afterwards. Each data point corresponds to a new coupon to avoid cross-measurement artifacts [22, 23].

Figures 2(a)–(c) shows the evolution in overall PL intensity and peak position after ambient-2 exposure. Two regimes are defined based on the linearity analysis provided in the supporting information (Supplementary figure 1). In the first regime, after 1 d of ambient-2 exposure, the intensity rapidly increases threefold and the peak redshifts 12 ± 2.7 meV. A peak shift is typically explained in one of two ways: (1) film straining or changing dielectric environment, which both modify the WS_2 band structure and shift the exciton and trion emissions [24]. (2) Charge-related modulation i.e. doping, which does not induce a shift in the exciton and trion emissions but changes the exciton and trion spectral weights [25]. Hence, exciton and trion emissions are extracted (methods) and their spectral weights and peak positions are reported in figure 2(b)—(d), respectively, to identify the origin of the shift in overall peak position. Figure 2(b) shows a decrease/increase in exciton/trion spectral weight over 1 d. Some example spectra with exciton and trion extractions are provided in the supporting information (Supplementary figure 2). In addition, figure 2(d) shows a redshift in in exciton and trion peak positions over 1 d. In the second regime, after 4–16 d of ambient-2 exposure, the WS_2 film exhibits maximum PL intensity which diminishes over 12 d. The overall peak position no longer shifts significantly, as shown in figure 2(c). This is also reflected in the exciton and trion spectral weights, which are scattered around 70%–60%/30%–40%, respectively. In addition, figure 2(d) reveals a small redshift in trion peak position in the range of 10 meV, while no significant shift is noted in exciton peak position.

In the first regime, the enhanced PL emission, trion to exciton weight increase and peaks' redshifts are very much

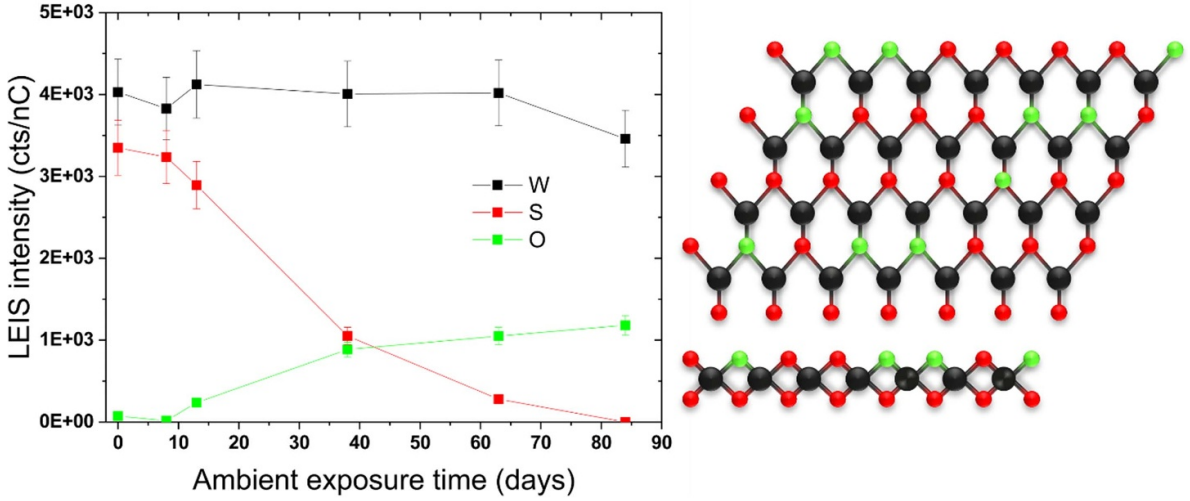

Figure 1. Aging of MOCVD grown monolayer WS_2 upon ambient exposure. Low energy ion scattering measurements of ambient-1 exposed monolayer WS_2 showing the substitution of sulfur by oxygen over time, while the tungsten backscattered ion yield remains constant. Schematic depiction of monolayer WS_2 illustrating the field of view for incident ions consists of tungsten atoms in between adjacent sulfur atoms, partially substituted by oxygen due to aging.

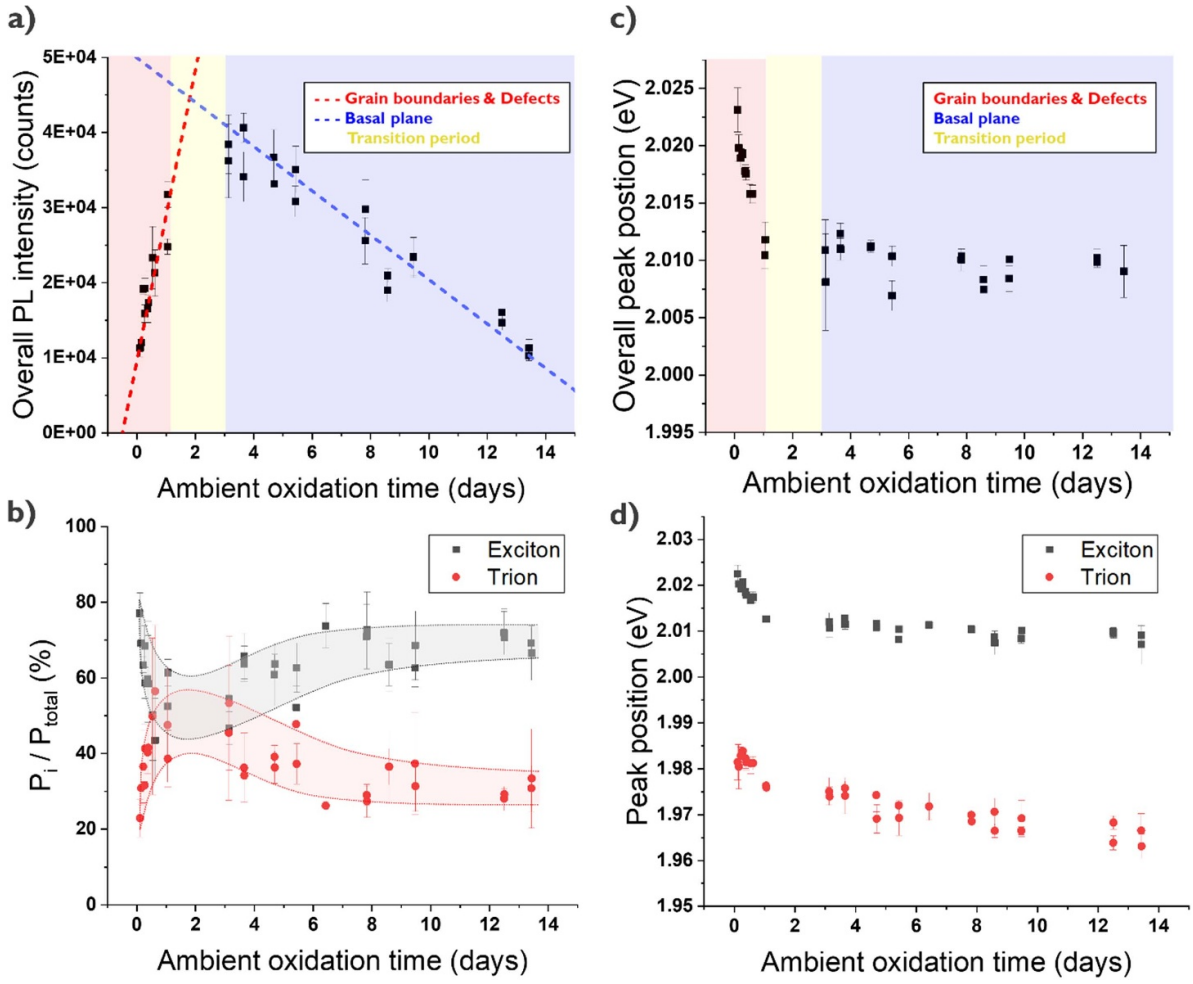

Figure 2. Effect of aging on the photoluminescent properties of monolayer WS_2. Evolution in (a) overall PL intensity and (b) exciton & trion peak contributions (c) overall PL peak position (d) exciton & trion peak positions.

line with the results of Zhang *et al* [23]. In their work, monolayer WS_2 was illuminated with a 532 nm laser in a 40% relative humidity environment, similar to the ambient-2 conditions in this work (supplementary figure 4). They experimentally demonstrated that these three changes in PL response originated from the interplay between physisorbed water, O_2 gaseous species and sulfur vacancies. Together with the learnings from other studies, a more comprehensive explanation is provided: Directly after growth, WS_2 films grown via MOCVD are known to contain some growth-related defects like grain boundaries and sulfur vacancies [26, 27]. Sulfur vacancies are most stable intrinsic defect [28–31] and induce defect generated subgap states (DGSS) that enable nonradiative recombination of excited carriers [15, 32–34]. These growth-related defects have a lower oxygen gas adsorption barrier compared to the basal plane [8, 10] and will oxidize first, removing their DGSS and thus enhancing the PL emission as shown in figure 2(a). Sulfur vacancy oxidation can also be responsible for the decrease/increase in exciton/trion spectral weight noted in figure 2(b), because of its effect on the prerequisites for trion formation i.e. (1) free charge carriers and (2) exciton availability. (1) DGSS act as reservoirs that take up free charge carries, thereby locally trapping the latter and reducing its density in the rest of the WS_2 film [35]. Moreover, at low electron density, the time scale for trion formation is much longer than the exciton lifetime [36], explaining the predominant exciton over trion weight, initially. (2) DGSS not only allow for nonradiative recombination, but also give rise to long-lived, immobile trapped excitons or charges which themselves act as nonradiative recombination centers for freely diffusing excitons, similar to a defect-mediated Auger recombination process [37]. Defect oxidation thus allows for better trion formation conditions by removing the DGSS and their effects. Finally, the PL redshift observed in figure 2(c) and (d) are attributed to the changing dielectric environment, resulting from phyisorbed O_2 and water vapor [23] and water intercalation [38]. It is widely known that the dielectric properties of the surrounding environment heavily influence the many-body effects that govern the PL characteristics of TMDC films, influencing electron–electron and electron–hole Coulomb interactions [25, 39]. This so-called dielectric screening effect affects both exciton and trion binding energies and the quasiparticle bandgap [40]. Intercalated water is known for its efficient dielectric screening, even though its dielectric constant is significantly smaller compared to bulk water due to the lower rotational freedom of water dipoles near surfaces [38, 41, 42]. Zhang *et al* unequivocally correlated PL redshifts with the presence of intercalated water [43]. Additionally, it has been demonstrated that physisorbed water and O_2 gaseous species induce PL peak shifts, which was also attributed to the changing dielectric constant near the WS_2 surface [23].

In the second regime, the PL maximum suggests most growth defects have been oxidized, from which the oxidation process proceeds further into the film [5, 9]. The slower rate at which the PL evolves suggests a different part of the film gets oxidized i.e. the basal plane which is known to have a larger kinetic barrier for O_2 gas adsorption and dissociation compared to grain boundaries or sulfur vacancies [10, 11]. Note the shorter time scale at which aging takes place compared to figure 1 likely results from the different types of ambient exposure, as explained in more detail in the methods section. The subsequent PL degradation indicates that, at a certain point, the increasing oxygen content in the film causes significant compositional changes that negatively impact PL emission. These significant compositional changes are also demonstrated by Rutherford backscattering spectroscopy (RBS) measurements, provided in the supporting information (Supplementary figure 3). The RBS measurements show a constant tungsten density, while the sulfur density initially decreases significantly but diminishes after 1 week. In addition, these significant compositional changes i.e. strong increase in oxygen film concentration also explains the overall larger exciton to trion spectral weight reported in figure 2(b). This is because, while physisorbed O_2 on the basal plane does not induce charge transfer [34], chemisorbed oxygen is known to lower the free carrier density in monolayer WS_2, which promotes exciton over trion formation [15, 44]. The small scattering in exciton and trion spectral weights is attributed to small variations in material quality, which is to be expected given the large-scale film growth (methods). Finally, the increasing oxygen concentration may also explain the additional PL i.e. trion redshift shown in figure 2(c) and (d), since the larger electronegativity of oxygen compared to sulfur changes the mechanical properties [45] and may cause some strain build-up in the WS_2 film.

2.3. Mitigation WS_2 aging via controlled storage environments

Aging mitigation is imperative since it significantly affects the WS_2 film composition and sought-after PL properties. Strategies to prevent aging typically involve encapsulation e.g. with h-BN [46] or organic layers like pyrene or graphene [47, 48]. However, capping layers complicate subsequent process steps, alter the TMDC layer's properties and may damage the latter upon removal [6]. An alternative strategy is therefore highly desirable. A 300 mm wafer of monolayer WS_2 grown via MOCVD on 90 nm SiO_2 (methods) is cut into coupons that are stored in various controlled environments. The controlled environments attempt to mitigate aging by limiting either of the essential elements for photo-induced oxidation; (1) limiting light exposure i.e. excitation events (Black FOUP) or (2) limiting oxygen availability (N_2-purged cabinet, glovebox, and desiccator). Detailed descriptions of the controlled environments are provided in the method section. Each measurement corresponds to a new coupon to avoid cross-measurement artifacts [22, 23].

Figure 3 shows the water contact angle (WCA), XPS characterization of the W4*f* core level, and overall PL intensity, monitoring film oxidation i.e. the aging process. The wettability of ambient-2 exposed WS_2 increases over 2 weeks, as

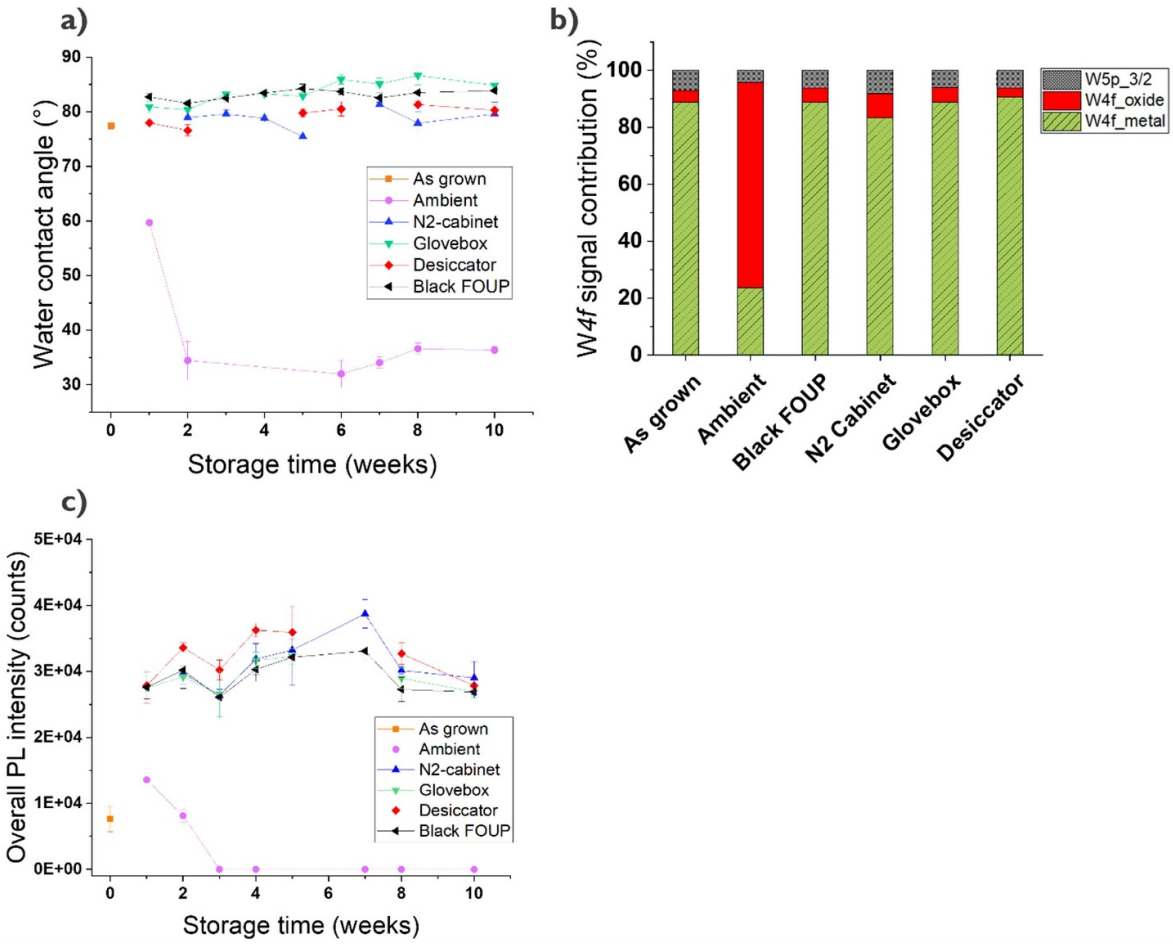

Figure 3. Aging mitigation via storage in controlled environments. Monolayer WS_2 stored in ambient and various controlled environments showing the evolution in (a) surface wettability (b) W4*f* signal contributions measured by XPS after 10 weeks and (c) PL intensity over 10 weeks.

shown in figure 3(a), after which the WCA stabilizes around 35°. In contrast, all controlled environments show a constant WCA over 10 weeks of storage. In addition, figure 3(b) reveals a strong increase in W_{oxide} chemical states after ambient-2 exposure compared to the as-grown film, while no significant change in chemical states manifests after 10 weeks in controlled environments, though a slightly higher W_{oxide} signal contribution is noted for the N_2-purged cabinet. The W4*f* spectra are provided in the supporting information (supplementary figure 5) and the analysis method is summarized in the methods section. Finally, aging mitigation is assessed with extreme sensitivity via PL spectroscopy, as shown in figure 3(c). After 1 week, all conditions show an enhanced PL intensity compared to the as-grown film. Subsequently, ambient-2 exposed WS_2 exhibits a linear PL decrease over 2–3 weeks, similar to the observations reported in figure 2(a), while the WS_2 films stored in controlled environments shows a rather stable PL response over 10 weeks.

The increasing surface hydrophilicity shown in figure 3(a) has been associated with WS_2 oxidation [49], reflecting the aging process. In addition, the time scale over which the aging transpires is in line with the trend previously observed in figure 2. The stable WCA measured for all controlled storage environments indicates no significant changes in WS_2 surface chemistry, demonstrating aging mitigation. The small variations in WCA between the controlled environments may be attributed to differences in volatile organic compounds layer build-up, which also affects the surface wettability [50, 51]. The W4*f* XPS results shown in figure 3(b) paint a similar picture, where the strong increase in W_{oxide} states after 10 weeks of ambient-2 exposure in comparison to the controlled environments and as-grown film demonstrate aging mitigation. Moreover, the slightly higher W_{oxide} signal contribution noted for the N_2-purged cabinet indicates an inferior storage quality. The storage quality of the oxygen-controlled environments is evaluated based on the O_2 gas concentration and relative humidity (supplementary figure S4). Although the aforementioned oxidation mechanism proposed by Chang *et al* only involves O_2 gas [6], water vapor might also play a role in the aging process as reported by Atkin *et al* [52]. The N_2-purged cabinet holds both a larger O_2 gas concentration and relative humidity compared to other oxygen-controlled environments. Thus, the inferior storage quality of the N_2-purged cabinet results from the larger oxygen availability, which enhances

basal oxidation that is otherwise more kinetically limited [10, 11]. Finally, the overall higher PL intensity after 1 week compared to the as-grown film, noted in figure 3(a), suggests some aging occurred for both ambient exposed and controlled environments. The subsequent PL degradation observed for ambient-2 exposed WS_2 is in line with the observations in figure 2(a), indicating significant aging. In addition, the PL enhancement observed for all controlled environments is similar to the observations of regime 1 reported in figure 2(a), related to sulfur vacancy oxidation. Also, similar exciton- and trion weights and peak positions over 10 weeks of storage are observed (supplementary figure 6), in line with the trends reported in figures 2 (b)–(d). Moreover, the relatively stable PL response between weeks 1–10 suggests no significant additional aging takes place. The small intensity variations are attributed to limited variability in the WS_2 film quality over the 300 mm wafer. Even though the XPS results for the N_2-purged cabinet indicate slightly more aging, there are no significant differences in absolute PL intensity compared to the other controlled environments. Extending the time scale of the experiment and increasing measurement frequency would help in better differentiating between the different storage environments based on their quality. Unfortunately, this could not be done in the present study due to coupon shortage, but, nevertheless, the current data shows that storage in controlled environments leads to significant aging mitigation and preservation of the WS_2 film quality. Based on these PL observations, authors conclude that sulfur vacancies will oxidize even upon limited ambient-2 exposure, being a highly thermodynamically favorable process [10, 11]. However, further WS_2 aging can be mitigated by (1) limiting excitation events (i.e. light exposure) required for the photo-induced oxidation or (2) limiting oxygen availability i.e. take advantage of the slow kinetics that rule basal plane oxidation. Ultimately, aging-induced film degradation that occurs in a timespan of days (figure 2) can be mitigated by storing the WS_2 film in a controlled environment that stabilizes the PL emission and layer composition, as demonstrated by WCA and XPS measurements, over a timespan of months.

3. Methods

3.1. WS_2 growth

Monolayer WS_2 was synthesized using a MOCVD process on 300 mm silicon wafers with 90 nm of thermally grown oxide on top. The wafer was gradually heated inside the chamber to 750 °C under a flow of high-purity N_2/H_2 gases. Film growth was initiated by introducing $W(CO)_6$ and H_2S gases into the chamber (precursor partial pressures ratio $H_2S/W(CO)_6 = 5 \times 10^3$) for 10 min at a chamber pressure of 150 Torr. Subsequently, layer closure was promoted by lowering the chamber pressure to 20 Torr and increasing the temperature to 900 °C. A high resolution 1×1 um^2 atomic force microscopic image can be found in the supporting information (supplementary figure 7).

3.2. Atomic force microscopy

The AFM scan shown in supplementary figure 7 was recorded with a Nanoscope V AFM tool (Bruker) using a HQ-NSC19/AIBs cantilever in PeakForce Quantitative Nanomechanics mode. The latter allows for direct control over the peak normal force and minimal lateral force which makes it a non-destructive, high-resolution imaging method with no ambiguity regarding the image contrast since the force distance data is directly analyzed.

3.3. LEIS

LEIS measurements were performed after heating the samples to 200 °C to remove the volatile organic compounds and have the surface of interest exposed. Measurements were carried out at IONTOF GmbH where the measurements were performed using $^4He^+$ as primary ions at normal incidence with an ion energy of 3 keV and an ion current of 5.7 nA. Each spectrum was acquired bases on an analysis area of 2×2 mm^2 with an ion fluence of 5 10^{13} ions cm^{-2} for 55 s. The scattered ions were analyzed using a double toroidal energy analyzer, accepting ions with a backscattering (polar) angle of 145°, with full acceptance over the azimuthal angle.

3.4. Steady-state PL spectroscopy

The recorded PL spectrum heavily depends on the measurement settings, such as temperature, ambient conditions, laser wavelength, laser power, to name a few [14, 25]. In this study, the monolayer WS_2 photoluminescent response was measured with a Horiba Jobin-Yvon HR800 system at room temperature with a 532 nm laser, 0.05 mW laser power (or 1% ND filter), 1000 μm confocal hole, 600 grooves/mm grating, 100×0.9 NA Olympus objective, and a double exposure of 1 (accumulations) $\times$ 10 s (integration time) with spike filter to eliminate cosmic spikes. These measurements settings are widely used in literature since it allows to generate electron–hole pairs, while minimizing excessive energy that could damage the WS_2 film via local heating [25, 53].

Not only variations in measurements settings, but also differences in post spectrum processing complicate cross-study comparisons. Most studies use two components i.e. exciton and trion emissions, but vary in the mathematical models used e.g. Gaussian [54], Lorentzian [55] or Voigt [56]. Additionally, some studies add extra components to their fitting related to SiO_2 hole-trap assisted defect-induced exciton species [57], localized states [58] and bi-excitons [59]. Consequently, authors believe there is no consensus regarding the spectral deconvolution in the current literature.

Using the Origin™ software, a first peak (Voigt) was manually added near maximum intensity, after which a second peak (Voigt) at lower energy was included to achieve an acceptable fitting. Hence, the spectral deconvolution in this study was limited to two components i.e. exciton and trion emissions. In addition, another fitting requirement was that the

energy difference between the exciton and trion components needed to be approximately 40 meV, as shown in figure 2(d), which is both theoretically and experimentally reported [36]. Note that the missing data points shown in figure 3(c) result from discarding specific coupons based on the physical damage suffered during cleaving or mishandling during collection.

3.5. RBS

Rutherford backscattering spectroscopic measurements were performed using a 6SDH tandem accelerator (National Electrostatics Corporation) to accel He^+ ions that were magnetically analyzed to determine the ion energy and eliminate contaminants. An ion energy of 1.523 MeV with 22 nA beam current was used and the beam collimated to 1 mm before introduction in the scattering chamber, where the sample was mounted at a tilt angle of 11° and scattering angle of 170°. The detector was calibrated with a 68 KeV offset, 1.4925 KeV gain and a FWHM of 0.01626 MeV.

The error bars reported resemble the absolute error, calculated via the formula:

$$\sqrt{\left(\frac{\text{Sum}}{4}\right)^2 + (\text{Sum}*0.02)^2}$$

where Sum represents the elemental fitting value i.e. the amount of the element in atoms cm^{-2}.

3.6. WCA

Wettability measurements were performed using an OCA contact angle system (Dataphysics) with a standard CCD camera (768 x 576 25 fps intercalated) and Hamilton 500 μL syringe with a needle thickness of 0.52 mm. Surface wettability was assessed via a static WCA method i.e. the water droplet was manually dispensed onto the WS_2 surface, after which the droplet was allowed to reach its equilibrium wetting. A snapshot was taken after 30 s and was used to calculate the contact angle of the water droplet and WS_2 surface. Note that the missing data points shown in figure 3(a) result from discarding specific coupons based on the physical damage suffered during cleaving after growth or mishandling during collection.

3.7. X-ray photoelectron spectroscopy

The XPS measurements were carried out using a monochromatized photon beam of 1486.6 eV with a 100 μms spot size with charge neutralization in an Angle Integrated mode using a QUANTES instrument from Physical electronics.

CasaXPS software was used to analyze and deconvolute the W4*f* spectra. In case of the W4*f* core level, the spectra were deconvoluted by fitting doublets corresponding to W(0) i.e. WS_2 at ± 32 & 34 eV, W(+IV) i.e. WO_2 at ± 34 & 36 eV and W(+VI) i.e. WO_3 at ± 35.3 & 37.8 [60], while respecting an area ratio of ¾ resulting from spin–orbit coupling [61]. An extra peak was added at high binding energy corresponding to the W5$p_{3/2}$ subshell [60]. A Lorentzian asymmetric line shape was used to extract the different peak contributions and normalized to account for any acquisition-related intensity variations. The deconvoluted spectra together with the peak numerical values are provided in the supplementary figure 5.

3.8. Ambient environments

Throughout this study two types of 'ambient conditions' are defined depending on the experiment. The data shown in figure 1 resulted from ambient-1 exposure which corresponds to daylight (±7 h day^{-1} exposure) in an uncontrolled environment (no special monitoring of the O_2 gas concentration and relative humidity). The data reported in figures 2 and 3 resulted from ambient-2 exposure which corresponds to continuous (24 h day^{-1}) white light exposure in a controlled lab/cleanroom environment (supplementary figure 4). The different types of light exposure explain the different time scales for WS_2 aging observed in figures 1 and 2, spiking the interest in the effect of light fluence on the aging dynamics. Future work should focus on (1) the effect of light fluence and 2) different O_2 gas or humidity levels on the aging rate.

3.9. Light limited storage environment

A non-transparent, black front opening unified pod (FOUP) was used to verify the effect of limiting light exposure on the aging process. The WS_2 coupons were placed on a pocket wafer inside the FOUP and collected for measurements, while minimizing the FOUP opening time i.e. exposure to the white light of the clean room.

3.10. Oxygen limited storage environments

The N_2-purged cabinet, glovebox and desiccator were all closed off systems, but with a transparent cover i.e. exposure to white light of the cleanroom. The WS_2 coupons were placed in sample boxes and collected for measurements, while minimizing the opening time for the N_2-purged cabinet and desiccator i.e. exposure to clean room ambient. The glovebox consisted of a load-lock system i.e. coupons stored in this system were never again exposed to ambient after initial storage.

3.11. Quality assessment of O_2 controlled environments

A GX-6000 gas monitor was used to measure the O_2 gas concentration and relative humidity in combination with EasyLog USB for data analysis. The O_2 gas concentration and relative humidity reported correspond to the environments in steady state i.e. the measurement was performed 3–5 min after introduction of the gas monitor into the controlled environment.

4. Conclusion

In summary, 2D TMDC layers, such as MOCVD grown monolayer WS_2, are prone to aging i.e. spontaneous oxidation upon ambient exposure as demonstrated by RBS and LEIS measurements, showing the gradual substitution of sulfur by oxygen atoms.

In the first hours of ambient exposure, the change in overall composition remains negligible i.e. below the sensitivity limits of surface analysis techniques and aging enhances the PL by oxidizing growth-related defects such as sulfur vacancies, thereby eliminating DGSS and their effects. Beyond 2–4 d of ambient exposure (∼3 d in controlled lab conditions with 24 h of white light exposure, ∼10 d in daylight), the compositional changes start to dominate, gradually diminishing the photoluminescent signal over time.

Aging can be mitigated without a capping layer by storing the WS_2 monolayer in controlled environments that either limit light exposure or the availability of the oxygen source (O_2 gas & humidity). As a result, the film quality and photoluminescent response no longer degrades over a time scale of days, as is the case upon ambient exposure, but remains stable over months. When it comes to long term storage in oxygen-controlled environments, more aging takes place when the oxygen source is more readily available. Although the aging dynamics are chalcogen dependent, authors expect these mitigation strategies to be universally applicable given the common, photo-induced nature of the aging process.

These learnings highlight the importance of proper 2D TMDC storage, especially synthetic layers deposited by MOCVD; authors recommended to store these films in non-transparent containers or environments that are O_2 and moisture free and encourage future studies to provide a statement in the methods section describing their storage protocol.

Data availability statement

All data that support the findings of this study are included within the article (and any supplementary files).

Acknowledgments

The project leading to this publication has received funding from the European Union's Horizon 2020 research and innovation program Graphene Flagship 2D Experimental Pilot Line (2D-EPL), Grant no. 952792.

Author contributions

The manuscript was written by P-J Wyndaele with contributions from J-F de Marneffe and S De Gendt. The manuscript was revised and approved by all co-authors. P-J Wyndaele carried out the photoluminescence measurement and was in involved in the coordination of the XPS and RBS characterization and all data processing and analysis. J-F de Marneffe was involved in all discussions regarding data analysis and interpretation. R Slaets performed the WCA measurements and storage environment quality assessments and was involved in the data analysis. B Groven was responsible for the WS_2 material growth and was involved in the data analysis. P Brüner and T Grehl were involved in the coordination and execution of the LEIS measurements and data analysis. S De Gendt was involved in all discussions involving data analysis and interpretation.

Conflict of interest

The authors declare no competing financial or non-financial interests.

ORCID iDs

P-J Wyndaele https://orcid.org/0000-0003-4010-8377
T Grehl https://orcid.org/0000-0003-1591-8490

References

[1] Akinwande D, Huyghebaert C, Wang C-H, Serna M I, Goossens S, Li L-J, Wong H-S P and Koppens F H L 2019 Graphene and two-dimensional materials for silicon technology *Nature* **573** 507–18
[2] Das S *et al* 2021 Transistors based on two-dimensional materials for future integrated circuits *Nat. Electron.* **4** 786–99
[3] Pramoda K and Rao C N R 2022 Two-dimensional materials and their hetero-superlattices for photocatalytic hydrogen evolution reaction *Chem. NanoMat* **8** e202200153
[4] Fu Y *et al* 2022 Layer structured materials for ambient nitrogen fixation *Coord. Chem. Rev.* **460** 214468
[5] Kotsakidis J C, Zhang Q, Vazquez de Parga A L, Currie M, Helmerson K, Gaskill D K and Fuhrer M S 2019 Oxidation of monolayer WS_2 in ambient is a photoinduced process *Nano Lett.* **19** 5205–15
[6] Chang Y-P, Li W-B, Yang Y-C, Lu H-L, Lin M-F, Chiu P-W and Lin K-I 2021 Oxidation and degradation of WS_2 Monolayers grown by nacl-assisted chemical vapor deposition: mechanism and prevention *Nanoscale* **13** 16629–40
[7] Martincová J, Otyepka M and Lazar P 2017 Is Single Layer MoS2 Stable in the Air? *Chem. - Eur. J.* **23** 13233–9
[8] Rong Y, He K, Pacios M, Robertson A W, Bhaskaran H and Warner J H 2015 Controlled preferential oxidation of grain boundaries in monolayer tungsten disulfide for direct optical imaging *ACS Nano* **9** 3695–703
[9] Pető J, Ollár T, Vancsó P, Popov Z I, Magda G Z, Dobrik G, Hwang C, Sorokin P B and Tapasztó L 2018 Spontaneous doping of the basal plane of MoS 2 single layers through oxygen substitution under ambient conditions *Nat. Chem.* **10** 1246–51
[10] Kc S, Longo R C, Wallace R M and Cho K 2015 Surface oxidation energetics and kinetics on MoS_2 monolayer *J. Appl. Phys.* **117** 135301
[11] Longo R C, Addou R, KC S, Noh J-Y, Smyth C M, Barrera D, Zhang C, Hsu J W P, Wallace R M and Cho K 2017 Intrinsic air stability mechanisms of two-dimensional transition metal dichalcogenide surfaces: basal versus edge oxidation *2D Mater.* **4** 025050
[12] Shukla V, Stone A, McGrath M, Kane A and Hurt R 2022 Chemical degradation kinetics for two-dimensional materials in natural and biological environments—a data-driven review *Environ. Sci. Nano* **9** 2297–319
[13] Liu H, Han N and Zhao J 2015 Atomistic insight into the oxidation of monolayer transition metal dichalcogenides: from structures to electronic properties *RSC Adv.* **5** 17572–81
[14] Tebyetekerwa M, Zhang J, Xu Z, Truong T N, Yin Z, Lu Y, Ramakrishna S, Macdonald D and Nguyen H T 2020 Mechanisms and applications of steady-state photoluminescence spectroscopy in two-dimensional transition-metal dichalcogenides *ACS Nano* **14** 14579–604

[15] Cui Q *et al* 2021 Robust and high photoluminescence in WS_2 Monolayer through in situ defect engineering *Adv. Funct. Mater.* **31** 2105339

[16] Gao J, Li B, Tan J, Chow P, Lu T M and Koratkar N 2016 Aging of transition metal Dichalcogenide monolayers *ACS Nano* **10** 2628–35

[17] Nan H *et al* 2014 Strong photoluminescence enhancement of MoS2 through defect engineering and oxygen bonding *ACS Nano* **8** 5738–45

[18] Cushman C V, Brüner P, Zakel J, Major G H, Lunt B M, Smith N J, Grehl T and Linford M R 2016 Low energy ion scattering (LEIS). A practical introduction to its theory, instrumentation, and applications *Anal. Methods* **8** 3419–39

[19] Brongersma H H, Draxler M, de Ridder M and Bauer P 2007 Surface composition analysis by low-energy ion scattering *Surf. Sci. Rep.* **62** 63–109

[20] Primetzhofer D, Markin S N, Efrosinin D V, Steinbauer E, Andrzejewski R and Bauer P 2011 Influence of screening length modification on the scattering cross section in LEIS *Nucl. Instrum. Methods Phys. Res.* B **269** 1292–5

[21] Li Q, Zhou Q, Shi L, Chen Q and Wang J 2019 Recent advances in oxidation and degradation mechanisms of ultrathin 2D materials under ambient conditions and their passivation strategies *J. Mater. Chem.* A **7** 4291–312

[22] Li Y *et al* 2021 Unraveling the synergetic mechanism of physisorption and chemisorption in laser-irradiated monolayer WS_2 *Nano Res.* **14** 4274–80

[23] Zhang H, Dunklin J R, Reid O G, Yun S J, Nanayakkara S U, Lee Y H, Blackburn J L and Miller E M 2020 Disentangling oxygen and water vapor effects on optoelectronic properties of monolayer tungsten disulfide *Nanoscale* **12** 8344–54

[24] Chaves A *et al* 2020 Bandgap engineering of two-dimensional semiconductor materials *npj 2D Mater. Appl.* **429**

[25] Gao M, Yu L, Lv Q, Kang F, Huang Z H and Lv R 2023 Photoluminescence manipulation in two-dimensional transition metal dichalcogenides *J. Mater.* **9** 768–86

[26] Delie G, Chiappe D, Asselberghs I, Huyghebaert C, Radu I, Banerjee S, Groven B, Brems S and Afana'ev V V 2021 Processing stability of monolayer WS_2 on SiO_2 *Nano Express* **2** 1–8

[27] Zheng W *et al* 2022 Defect-induced distinct exciton-exciton interactions in WS_2 monolayers *Sci.China Mater.* **65** 2502–10

[28] Kim J Y, Gelczuk Ł, Polak M P, Hlushchenko D, Morgan D, Kudrawiec R and Szlufarska I 2022 Experimental and theoretical studies of native deep-level defects in transition metal dichalcogenides *npj 2D Mater. Appl.* **675**

[29] Hong J *et al* 2015 Exploring atomic defects in molybdenum disulphide monolayers *Nat. Commun.* **6** 1–8

[30] Zhou W, Zou X, Najmaei S, Liu Z, Shi Y, Kong J, Lou J, Ajayan P M, Yakobson B I and Idrobo J-C 2013 Intrinsic structural defects in monolayer molybdenum disulfide *Nano Lett.* **13** 2615–22

[31] Komsa H P and Krasheninnikov A V 2015 Native defects in bulk and monolayer MoS_2 from first principles *Phys. Rev.* B **91** 1–17

[32] Singh A and Singh A K 2021 Atypical behavior of intrinsic defects and promising dopants in two-dimensional WS_2 *Phys. Rev. Mater.* **5** 2–10

[33] Bui V Q, Pham T T, Le D A, Thi C M and Le H M 2015 A first-principles investigation of various gas (CO, H_2O, NO, and O_2) absorptions on a WS_2 monolayer: stability and electronic properties *J. Phys.: Condens. Matter* **27** 305005

[34] Bianchi M G, Risplendi F, Re Fiorentin M and Cicero G 2024 Addressing the effects of gas adsorption on monolayers beyond charge population analysis: the case of WS_2 *npj Comput. Mater.* **10** 62

[35] Zhang T and Wang J 2021 Defect-enhanced exciton-exciton annihilation in monolayer transition metal dichalcogenides at high exciton densities *ACS Photonics* **8** 2770–80

[36] Ayari S, Jaziri S, Ferreira R and Bastard G 2020 Phonon-assisted exciton/trion conversion efficiency in transition metal dichalcogenides *Phys. Rev.* B **102** 125410

[37] Goodman A J, Lien D-H, Ahn G H, Spiegel L L, Amani M, Willard A P, Javey A and Tisdale W A 2020 Substrate-dependent exciton diffusion and Annihilation in chemically treated MoS_2 and WS_2 *J. Phys. Chem.* C **124** 12175–84

[38] Serron J *et al* 2023 Conductivity enhancement in transition metal dichalcogenides: a complex water intercalation and desorption mechanism *ACS Appl. Mater. Interfaces* **15** 26175–89

[39] Yuan Z, Hou J and Liu K 2017 Interfacing 2D semiconductors with functional oxides: fundamentals, properties, and applications *Crystals* **7** 1–22

[40] Man P, Srolovitz D, Zhao J and Ly T H 2021 Functional grain boundaries in two-dimensional transition-metal dichalcogenides *Acc. Chem. Res.* **54** 4191–202

[41] Fumagalli L *et al* 2018 Anomalously low dielectric constant of confined water *Science* **360** 1339–42

[42] Kim Y, Kang H, Song M, Kwon H and Ryu S 2023 Interfacial-water-modulated photoluminescence of single-layer WS_2 on Mica *Int. J. Mol. Sci.* **24** 3492

[43] Zhang Q, Lu J, Wang Z, Dai Z, Zhang Y, Huang F, Bao Q, Duan W, Fuhrer M S and Zheng C 2018 Reliable synthesis of large-area monolayer WS_2 single crystals, films, and heterostructures with extraordinary photoluminescence induced by water Intercalation *Adv. Opt. Mater.* **6** 1–9

[44] Tao Y, Yu X, Li J, Liang H, Zhang Y, Huang W and Wang Q J 2018 Bright monolayer tungsten disulfide: via exciton and trion chemical modulations *Nanoscale* **10** 6294–9

[45] Islam Z and Haque A 2021 Defects and grain boundary effects in MoS_2: a molecular dynamics study *J. Phys. Chem. Solids* **148** 109669

[46] Ahn S, Kim G, Nayak P K, Yoon S I, Lim H, Shin H-J and Shin H S 2016 Prevention of transition metal dichalcogenide photodegradation by encapsulation with h-BN Layers *ACS Nano* **10** 8973–9

[47] Canton-Vitoria R, Sayed-ahmad-baraza Y, Humbert B, Arenal R, Ewels C P and Tagmatarchis N 2020 Pyrene coating transition metal disulfides as protection from photooxidation and environmental aging *Nanomaterials* **10** 1–15

[48] Wyndaele P J *et al* 2024 Enhancing dielectric passivation on monolayer WS_2 via a sacrificial graphene oxide seeding layer *npj 2D Mater. Appl.* **8** 1–11

[49] Chow P K *et al* 2015 Wetting of mono and few-layered WS_2 and MoS_2 films supported on Si/SiO_2 substrates *ACS Nano* **9** 3023–31

[50] Kozbial A, Gong X, Liu H and Li L 2015 Understanding the intrinsic water wettability of molybdenum disulfide (MoS_2) *Langmuir* **31** 8429–35

[51] Khalkhali M, Zhang H and Liu Q 2018 Effects of thickness and adsorption of airborne hydrocarbons on wetting properties of MoS_2: an atomistic simulation study *J. Phys. Chem.* C **122** 6737–47

[52] Atkin P *et al* 2018 Laser exposure induced alteration of WS_2 monolayers in the presence of ambient moisture *2D Mater.* **5** 015013

[53] Peng Q *et al* 2021 Local laser heating effects in monolayer WS_2 probed by photoluminescence *Appl. Surf. Sci.* **562** 150226

[54] Harats M G, Kirchhof J N, Qiao M, Greben K and Bolotin K I 2020 Dynamics and efficient conversion of excitons to trions in non-uniformly strained monolayer WS_2 *Nat. Photon.* **14** 324–9

[55] Yang C *et al* 2020 All-optical reversible manipulation of exciton and trion emissions in monolayer WS_2 *Nanomaterials* **1023**
[56] Chow P K *et al* 2015 Defect-induced photoluminescence in monolayer semiconducting transition metal dichalcogenides *ACS Nano* **9** 1520–7
[57] Biswas C, Lee Y H, Sebait R, Song B and Seo C 2021 Identifying defect-induced trion in monolayer ws_2 via carrier screening engineering *ACS Nano* **15** 2849–57
[58] Xu W *et al* 2018 Determining the optimized interlayer separation distance in vertical stacked 2D WS_2:hBN:MoS_2 heterostructures for exciton energy transfer *Small* **14** 1–10
[59] Miakota D I, Unocic R R, Bertoldo F, Ghimire G, Engberg S, Geohegan D, Thygesen K S and Canulescu S 2022 A facile strategy for the growth of high-quality tungsten disulfide crystals mediated by oxygen-deficient oxide precursors *Nanoscale* **14** 9485–97
[60] Groven B, Tomczak Y, Heyns M, Radu I and Delabie A 2020 Two-dimensional WS_2crystals at predetermined locations by anisotropic growth during atomic layer deposition *J. Appl. Phys.* **128** 17530297
[61] Major G H *et al* 2020 Practical guide for curve fitting in x-ray photoelectron spectroscopy *J. Vac. Sci. Technol. A* **38** 061203